

Convective Heat Transfer Characteristics on End-Windings of Stator Immersed Oil-Cooled Electrical Machines for Aerospace Applications

Runyu Wang, Xinggang Fan, *Member, IEEE*, Dawei Li, *Senior Member, IEEE*, Ronghai Qu, *Fellow, IEEE*, Lei Li and Tianjie Zou

Abstract—The stator immersed oil cooling has emerged as a promising thermal management method for high power density electric machines applied in aerospace applications. However, due to the complex geometry of end-windings, the research on the convective heat transfer coefficient (CHTC) for the flooded stator is still at infancy. This paper investigates the convective heat transfer characteristics on end-windings of stator immersed oil-cooled electrical machines by computational fluid dynamics (CFD) methods and experiments implemented on a motorette. The variation law of the CHTCs of end-winding with flow rate is thoroughly investigated. Subsequently, new dimensionless correlations are defined using Nusselt numbers as a function of Reynolds numbers, which are further applied into a detailed lumped-parameter thermal network (LPTN) for rapid evaluation of temperature distribution. Finally, the obtained simulation results are verified by local temperature measurements. The experimental results also show that the proposed stator immersed oil-cooled structure can withstand a current density of up to 30A/mm² with a corresponding continuous power density of 6.8kW/kg.

Index Terms—Convective heat transfer characteristics, end-winding, high power density, stator immersed oil-cooled electrical machines.

NOMENCLATURE

$\lambda_{in}, \lambda_{im}$	Thermal conductivity of insulation and impregnation [W/(m·°C)].
V_{in}, V_{im}	The occupied volume of insulation and impregnation [m ³].
$\lambda_{im,in}$	Equivalent thermal conductivity of insulation and impregnation [W/(m·°C)].
R	Heat resistance [°C/W].
L	Heat transfer path length [m].
S	Effective heat transfer area [m ²].
r_1, r_2	Inner and outer radii of the sector [m].
α	Angle of the sector [°].
λ_p	Equivalent thermal conductivity of impregnation varnish containing air voids [W/(m·°C)].
x	Impregnation goodness.
δ_{in}	Thickness of the insulating layer [m].
r_c	Conductor radius [m].
\bar{u}	Time-averaged component [m/s].
u'	Pulsating component [m/s].
ρ	Density [kg/m ³].
t	Time [s].
p	Pressure [Pa].
μ	Fluid dynamic viscosity [kg/(m·s)].
v^*	Friction velocity [m/s].
τ_w	Wall shear stress [Pa].
y	Normal distance to the wall [m].

C_p	Specific heat capacity [J/kg·°C].
ν	Kinematic viscosity [mm ² /s].
h	Convective heat transfer coefficient [W/(m ² ·°C)].
q	Heat flux [W/m ²].
T_s	Convective heat transfer surface temperature [°C].
T_{ref}	Average temperature of local fluid on convective heat transfer surface [°C].
Re	Reynold number [dimensionless].
Nu	Nusselt number [dimensionless].
Pr	Prandtl number [dimensionless].
u	Average flow velocity [m/s].
d	Equivalent diameter of the end space section [m].
l	Axial distance of inlet or outlet from the end-winding [m].
r_{si}, r_{so}	Inner and outer radii of stator [m].

I. INTRODUCTION

WITH the global drive of pursuing “Net Zero”, electrification has become an irreversible trend within the transportation industry. At the very heart of electrified power trains is the electric machine. Many countries and enterprises have made ambitious commitments on the development of electric machines for automotive traction and aerospace propulsion with the focus on disruptively increasing their power density levels [1]-[3]. The Department of Energy (DoE) in the US has set a goal of achieving a power density of 33kW/L for 100kW electric traction drive systems by 2025 [4]. The next generation of aerospace propulsion electrical machines planned by NASA also targets on ultra-high power density of 13kW/kg [5]. This is pushing the boundaries of next generation machine developments in terms of increasing both torque density and rotation speed. Meanwhile, the resultant high power loss density will inevitably increase the risks of damaging the thermally vulnerable components due to overheating, which further threatens the reliability of machine’s operation and reduces their in-service lifetime [6] [7]. Therefore, thermal management has become more and more important for the design of high power density electrical machines.

Based on the adoption of different cooling media, the cooling methods of electrical machines can be classified into gas cooling and liquid cooling. With higher thermal conductivity and mass density, liquid is stronger than gas as coolant, with usually higher convective heat transfer coefficient (CHTC). Therefore, forced liquid cooling is more suitable for thermal management of high power density electrical machines, such as housing water jacket cooling [8] and direct oil cooling [9]. It should be noted that water is non-insulated and thus can only be used for indirect cooling. As shown in Table I and Fig. 1

TABLE I
TYPICAL VALUES FOR DIFFERENT COOLING METHODS [10]

Cooling method		Tangential stress [kPa]	Linear current density [kA/m]	Current density [A/mm ²]	Heat transfer coefficient [W/(m ² ·°C)]
Natural convection		-	-	1.5-5	5-30
Forced gas cooled	Air	<15	<80	5-10	20-300
	Hydrogen	<25	70-110	7-12	100-1000
	Indirect	20-60	90-130	7-20	100-10000
Forced liquid cooled	Direct	60-100	100-200	10-30	200-25000
	Phase change				500-50000

[10]-[15], the ultimate electrical load parameters of the electrical machines with indirect cooling are lower than those of the electrical machines with direct cooling. This is due to the long heat transfer path between the coolant and the heat source for indirect cooling, as well as the inability to fully contact the surface of the heat source [10]. Hence, direct oil cooling is the preferred cooling method for ultra-high power density electrical machines, especially the ones used for aerospace propulsion. Several studies have been carried out on the direct oil cooling method for high power density electrical machines. T. Davin proposed an oil-injected cooled structure for the end-windings that dissipated 2.5 to 5 times more heat than air cooling [16]. K. Lee used coolant-holes in hollow-shaft to splash the oil to cool the stator end-windings [17]. Z. Li developed the spray cooling method for electric machines, which sprays oil on the stator end-windings and rotor via nozzles [18]. Although oil-injected cooling and oil splash cooling consume less oil, they both have a strong cooling effect only on the end-windings, which leads to uneven cooling of the windings. A. Al-Timimy presented an oil-cooled system that can completely flood the stator and rotor [19]. However, the rotation of the rotor could result in significant friction loss on the surface of the rotor, reducing the efficiency of the electrical machine. Therefore, a sleeve is inserted between the stator and the rotor, and only immerses the stator in the oil [20]. A. L. Rocca proposed a stator immersed oil-cooled structure with yoke oil passages and slot oil passages for an aero engine starter generator system, enabling electrical machines with a power density of 11.85 kW/L [21].

Accurate CHTCs are the prerequisite for precise and rapid calculation of electrical machine temperature fields by lumped parameter thermal network (LPTN) and the finite element method (FEM). K. Bennion investigated the end-winding convective heat transfer for oil-injected cooling and analyzed the effect of inlet oil temperature and winding size on the CHTC [22]. C. Liu explored the influence of nozzle type, flow rate, pressure, and number of nozzles on the CHTC of the end-windings [23]. S. Kapatral performed two-phase flow simulation and analyzed the convective heat transfer characteristics of the end-winding using the volume of fluid (VOF) in CFD for rotating shaft splashing oil cooling [24]. Based on the existing research work as introduced above, the convective heat transfer characteristics of oil-injected cooling and oil splash cooling have been studied. However, the research on the convective heat transfer characteristics and relevant empirical correlations of the end-windings for stator immersed oil-cooled electrical machines is still in its infancy.

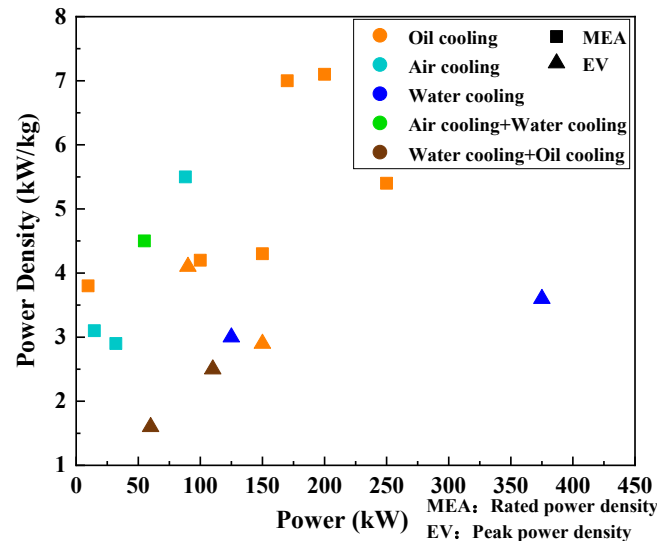


Fig. 1. Performance comparison of different cooling methods [10]-[15].

In this paper, the convective heat transfer characteristics of the end-winding for stator immersed oil-cooled electrical machines are comprehensively analyzed. An advanced thermal cooling structure with longitudinal staggered yoke oil passages and in-slot oil passages is proposed, and the corresponding electromagnetic performance of the electrical machine is presented in Section II. Based on the geometric dimensions of the machine, a single-tooth oil-cooled motorette model featuring an equivalent cooling structure is built for more efficient numerical analysis in Section III. Thereafter, the convective heat transfer characteristics and dimensionless empirical correlations of the end-windings for the stator immersed oil-cooled electrical machine are analyzed in Section IV. Meanwhile, the advantages in heat dissipation of the longitudinal and staggered yoke oil passages are also detailed in this section. The obtained simulation data is further verified by oil cooling experiments on the motorette in Section V. Moreover, the results of the dimensionless correlation calculations are integrated into a detailed thermal circuit which is verified using experimental measurements of local temperatures. Finally, a brief summary of this paper is proposed in Section VI.

II. STUDIED STATOR IMMersed OIL-COOLED ELECTRICAL MACHINES

A. Electromagnetic Parameters

In this paper, a stator immersed oil-cooled structure with efficient heat dissipation is proposed for high power density

permanent magnet synchronous motors (PMSMs). An 18-slot 12-pole PMSM with double-layer fractional slot concentrated winding (FSCW) is adopted for case study, as shown in Fig. 2. The benefits of FSCW are low cogging torque, short end-windings, and low copper loss. Meanwhile, the end-windings do not overlap with each other, allowing for electromagnetic and thermal isolation to increase fault tolerance and winding cooling efficiency. In order to further improve the reliability of the electrical machine, the dual three-phase topology driven by two sets of three-phase inverter bridges is adopted. Halbach magnet arrays without ferromagnetic yoke are implemented in the rotor to improve the amplitude and sinusoidal level of the air-gap magnetic flux density, as well as to reduce weight. The trapezoidal topology also reduces the risk of demagnetization at the corners of the Halbach PMs since the inclined interfaces between adjacent magnets allow for smoother magnetic transitions between magnet boundaries. The split ratio, magnet pole arc, and magnet segmentation per pole have been optimized to maximize the power density. Detailed parameters of the analyzed machine are listed in Table II.

TABLE II

BASIC ELECTRICAL MACHINE PARAMETERS	
Parameters	Values
Rated power [kW]	130
Rated torque [Nm]	155
Rated speed [rpm]	8000
Slot/Pole number	18/12
Rotor outer diameter [mm]	164.4
Stator outer diameter [mm]	230
Slot depth [mm]	24.5
Tooth width [mm]	14
Air-gap radial length [mm]	0.8
Sleeve thickness [mm]	1
Core length [mm]	60
In-slot passage size [mm]	3.5*24.5
PM material	Sm2Co17
Stator lamination material	1J22
Sleeve material	Glass fiber
Rotor banding material	Carbon fiber

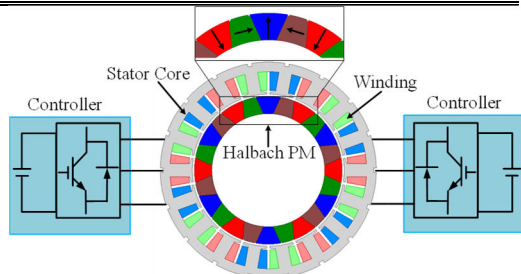


Fig. 2. Illustration of the machine topology and implementation of drives.

B. Cooling Structure

The stator immersed oil-cooled structure is implemented on a PMSM to demonstrate its efficient heat dissipation characteristics, as shown in Fig. 3. There are two pairs of inlet-outlet set-ups, with two inlets distributed 180° circumferentially from each other on the front endcap, and two outlets located on the rear endcap in the same way. A sleeve in contact with the stator inner surface is configured to separate

the stator and rotor space, with the aim of eliminating power loss and heat generated by the friction between the oil and the high-speed rotating rotor. Generally, glass fiber may be a preferred choice of stator sleeve material, in terms of comprehensive consideration of compressive strength and electrical conductivity. The sleeve is thickened near the end cap to enhance its mechanical strength, and both ends are sealed with high temperature resistant O-rings to guarantee a perfect sealing effect. To ensure that there is no local overheating of the stator, an oil separator is placed at the front end space to evenly distribute the flow in each oil passage. The oil separator has the same number of oil holes aligned with the end-windings as the number of slots, respectively.

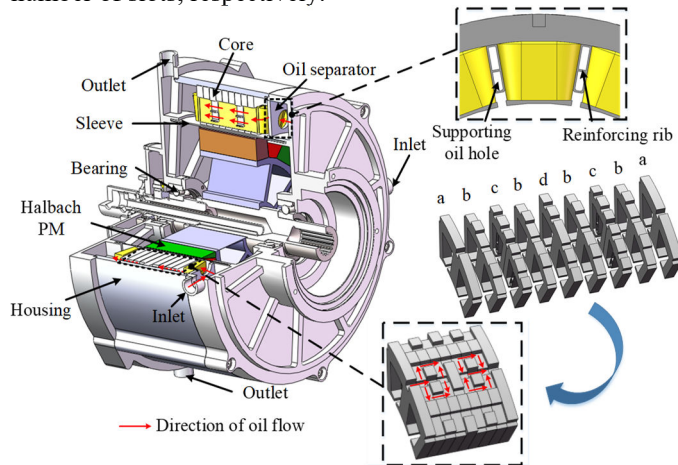


Fig. 3. Schematic of overall cooling structure.

The oil passages of the stator immersed oil-cooled structure can be formed in the yoke or between the coils in the slot, as well as even in the slot openings. The combination of different types of oil passages can also have an effect on the convective heat transfer in the end-windings. The stator immersed oil-cooled structure proposed in this paper is studied in the context of ultra-high power density electrical machines. Therefore, the cooling structure includes the above-mentioned oil passage types in order to achieve efficient heat dissipation, and the analyzed convective heat transfer characteristics of the end-windings are more relevant when having the same oil passage design. It is worth noting that the longitudinal and staggered yoke oil passages are presented in this paper, which increase the contact area between oil and yoke and further improve the heat dissipation performance of the yoke oil passages. The axial part of the longitudinal and staggered yoke oil passage is located at the centerline of the tooth due to the low magnetic flux density in this area. Furthermore, the depth of the local yoke oil passage along the circumferential direction is shallow. Therefore, the effect of the design of the longitudinal and staggered yoke oil passages on the electromagnetic performance of the machine can be almost neglected in this paper. The stator core is divided into 9 parts in the axial direction, and a total of 4 different shapes of iron core blocks are stacked to form longitudinal and staggered oil passages, as indicated by a-d in Fig. 3. Each type of core block is formed with yoke grooves and yoke protrusions with different shapes and could be manufactured by punching or wire cutting. In order to further increase the contact area

between the oil and the winding, in-slot oil passages are designed between the coils. In conventional FSCW PM machines, the space between coil to coil and coil to core is always limited due to the high filling factor of the conductors, enamel, and insulation resin, which would lead to blocked oil passages in the slots. Therefore, a supporting oil hole is configured between the two coils. In order to prevent the oil hole from being deformed, a reinforcing rib is arranged in the middle of the oil hole.

III. NUMERICAL MODEL AND LPTN MODEL OF MOTORETTE

A. Geometric Model

As the fluid-solid coupling simulation of full machine consumes a large number of computational resources, a reasonable simplification of the numerical model for the electrical machine is required. The flow in each oil passage of the electrical machine is evenly distributed due to the design of the oil separator. In addition, the FSCWs isolated from each other are used in the electrical machine. Therefore, according to the principle of circumferential symmetry, the stator immersed oil-cooled electrical machine can be simplified to a single-tooth, single-coil model as shown in Fig. 4.

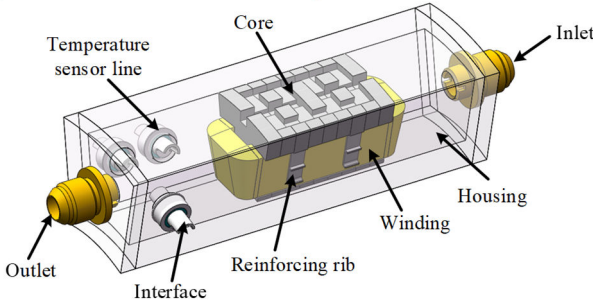


Fig. 4. Single-tooth winding motorette.

B. Equivalent Model of Winding

The establishment of the winding model is critical to the thermal analysis of the electrical machine. The winding as a heterogeneous body, consisting of copper conductors with insulation and impregnated varnish, is complex and time-consuming to model accurately [25]. Therefore, the equivalent thermal model of the winding is employed to accurately analyze the temperature of the winding, typically using the layer model [3] and the cubic model [26].

The layer model is used to equate the winding in the numerical model. The conductors of similar temperature are combined into the same copper layer. As shown in Fig. 5, an equivalent layer of insulation and impregnation is filled between two adjacent copper layers. The simplest layer winding model has only one copper layer and one equivalent layer of insulation and impregnation. Although this method is easy to model, it cannot accurately predict the maximum temperature and temperature gradient of the winding. Therefore, the multilayer winding model is used more widely, and the winding in this paper is divided into seven copper layers and seven impregnated and insulated layers. The equivalent thermal conductivity of the insulation and impregnation layers can be calculated using the following equation [27]:

$$\lambda_{im,in} = \lambda_{im} \frac{V_{im}}{V_{im} + V_{in}} + \lambda_{in} \frac{V_{in}}{V_{im} + V_{in}} \quad (1)$$

where $\lambda_{im,in}$ is the equivalent thermal conductivity of insulation and impregnation, λ_{in} , λ_{im} , V_{in} and V_{im} are the thermal conductivity and the occupied volume for insulation and impregnation, respectively.

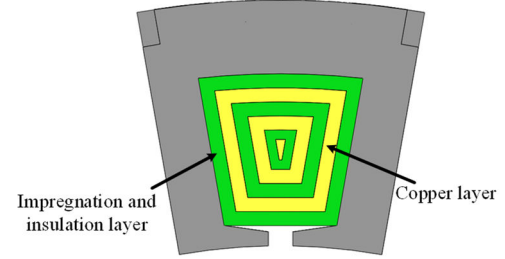


Fig. 5. The multilayer winding model.

Three-dimensional cubic models are used in LPTN model in this paper. As shown in Fig. 6, the winding is discretized into a number of cubic units, each of which creates a three-dimensional thermal network. The equations for calculating the thermal resistance in Fig. 6 are as follows:

$$R_{xyz1} = R_{xyz2} = \frac{L_{xyz}}{2\lambda_{xyz} S_{xyz}} \quad (2)$$

$$R_{xyz3} = -\frac{L_{xyz}}{6\lambda_{xyz} S_{xyz}} \quad (3)$$

where λ_{xyz} , S_{xyz} , L_{xyz} are the thermal conductivity, effective heat transfer area and heat transfer path length along x,y,z directions respectively.

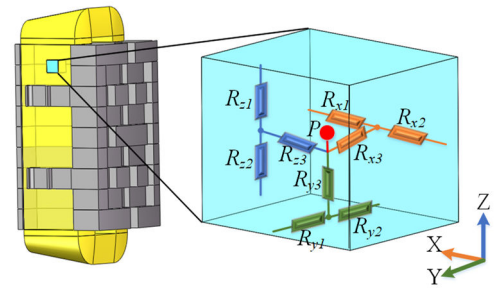


Fig. 6. Cuboidal element three-dimensional thermal network.

The end-winding can be equivalent to the sectoral heat path unit, with three-dimensional thermal resistances calculated by the following equation [28]:

$$R_{a1} = R_{a2} = \frac{180L_a}{\alpha\pi\lambda_a(r_2^2 - r_1^2)} \quad (4)$$

$$R_{a3} = -\frac{60L_a}{\alpha\pi\lambda_a(r_2^2 - r_1^2)} \quad (5)$$

$$R_{c1} = R_{c2} = \frac{\alpha\pi(r_1 + r_2)}{720\lambda_c L_a(r_2 - r_1)} \quad (6)$$

$$R_{c3} = -\frac{\alpha\pi(r_1 + r_2)}{6 \times 360\lambda_c L_a(r_2 - r_1)} \quad (7)$$

$$R_{r1} = \frac{90}{\alpha\pi\lambda_r L_a} \left[\frac{2r_2^2 \ln(r_2 / r_1)}{r_2^2 - r_1^2} - 1 \right] \quad (8)$$

$$R_{r_2} = \frac{90}{\alpha\pi\lambda_r L_a} \left[1 - \frac{2r_1^2 \ln(r_2/r_1)}{r_2^2 - r_1^2} \right] \quad (9)$$

$$R_{r_3} = \frac{-45}{\alpha\pi\lambda_r L_a (r_2^2 - r_1^2)} \left[r_2^2 + r_1^2 - \frac{4r_2^2 r_1^2 \ln(r_2/r_1)}{r_2^2 - r_1^2} \right] \quad (10)$$

where λ_a , λ_c , λ_r are the equivalent thermal conductivity along the axial, circumferential and radial directions, respectively. r_1 and r_2 are the inner and outer radii of the sector and α is the angle of the sector.

The three-dimensional thermal network involves the winding anisotropic thermal conductivity, which can be considered as composite materials to calculate. In addition, the winding impregnation goodness is difficult to reach 100%. Air voids will appear in the impregnation varnish, which will reduce the heat dissipation performance of the winding. After considering the air voids factor, the equivalent thermal conductivity of the winding can be expressed as [29]:

$$\lambda_{eq} = \frac{\pi\lambda_p / \sqrt{3}}{\ln\left(\frac{\sqrt{2\pi/V_{cu}}}{3^{1/4}} - 1\right) + \left(\frac{\lambda_p}{\lambda_m} \frac{4}{2 + \delta_m/r_c} - \frac{\sqrt{2\pi V_{cu}}}{3^{1/4}}\right) \frac{\delta_m}{r_c}} \quad (11)$$

$$\lambda_p = \lambda_m x + (1-x)\lambda_{air} \quad (12)$$

where λ_p is the equivalent thermal conductivity of impregnation varnish containing air voids, x is the impregnation goodness, δ_m is the thickness of the insulating layer, r_c is the conductor radius. In order to avoid the insulation damage caused by the long-term impact of oil, the winding surface is coated with a thin layer of thermal conductivity adhesive. The anisotropic thermal conductivity after comprehensive calculation is 0.6W/(m·°C), 0.6W/(m·°C) and 143.8W/(m·°C) respectively.

C. Numerical Model

This paper presents a numerical model based on CFD method for accurate prediction of fluid flow and convective heat transfer characteristics. CFD, as an important branch of fluid mechanics, is essentially a numerical method for solving a system of governing equations in fluid mechanics. All fluid-related phenomena in nature can be described by governing equations including the mass conservation equation, momentum conservation equation, and energy conservation equation. Considering the complex geometry of the end-winding studied in this paper, some vortices are generated during the flow of oil due to the blocking effect of the end-winding and the core. The vortices comprise local turbulence with chaotic and stochastic properties, and the pressure and velocity pulsations vary in time and space. The governing equations are transformed into the form of the following Reynolds Averaged Navier-Stokes (RANS) equations [30]:

$$\frac{\partial \bar{u}_i}{\partial x_i} = 0 \quad (13)$$

$$\frac{\partial(\rho \bar{u}_i)}{\partial t} + \frac{\partial(\rho \bar{u}_i \bar{u}_j)}{\partial x_j} = -\frac{\partial \bar{p}}{\partial x_i} + \frac{\partial}{\partial x_j} \left(\mu \frac{\partial \bar{u}_i}{\partial x_j} - \rho \overline{u'_i u'_j} \right) \quad (14)$$

where \bar{u} is the time-averaged component and u' is the pulsating component; ρ is the fluid density; t is the time; p is the

pressure; μ is the fluid dynamic viscosity and $-\rho \overline{u'_i u'_j}$ is the symmetric Reynolds stress tensor with six components.

Since the focus of this paper is on convective heat transfer characteristics, the standard $k-\varepsilon$ model and the shear stress transport (SST) $k-\omega$ model were chosen to be used because earlier studies [31]-[33] have proved the accuracy of these two models in computing fluid-solid coupling problems. However, the high Reynolds number $k-\varepsilon$ model is only valid in the fully developed flow region. In contrast, the $k-\omega$ model has better stability and accuracy in solving for fluids near the wall. The SST $k-\omega$ model uses the $k-\omega$ model at the near wall and the $k-\varepsilon$ model in the fully developed region, with a blending function to transform in between [34].

The mesh serves as the basis for discretization and has a significant impact on the results of numerical calculations. Fluent Meshing is used to split the mesh and optimize the poor quality meshes to ensure that the skewness and inverse-orthogonal quality of the mesh are both less than 0.9. The SST $k-\omega$ model employs a near-wall turbulence model to directly solve for the viscous sublayer in order to precisely quantify convective heat transfer at the fluid-solid interface. Compared to the wall function approach, the near-wall model requires a denser mesh at the boundary layer, and the dimensionless number y^+ is commonly employed to determine if the meshing of the near-wall region fits the requirements. The value of y^+ can be calculated by (15) and (16).

$$v_* = \sqrt{\frac{\tau_w}{\rho}} \quad (15)$$

$$y^+ = \frac{y \rho v_*}{\mu} \quad (16)$$

where v_* is friction velocity; τ_w is wall shear stress and y is the normal distance to the wall. In order to balance calculation time and accuracy, y^+ is required to be as close to 1 as possible. As shown in Fig. 6, the inflations are employed on the boundary surfaces between solid domain and fluid domain, and it has 10-layer mesh with a growth rate of 1.1. A mesh-independent analysis is required to assure the accuracy of the results, and the number of meshes in the final model is 14 million.

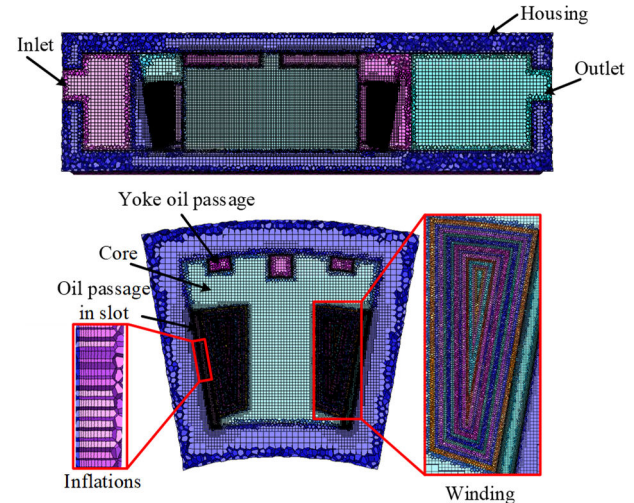


Fig. 7. Mesh of the single-tooth winding motorette.

The physical properties of each part of the motorette are shown in Table III. The coolant used is an aviation lubricant whose physical properties are derived from actual tests as an expression for the variation with temperature as shown in Table IV. The appropriate thermal boundary conditions for the coupled fluid-solid model are shown in Fig. 7. Constant temperature and mass flow boundary conditions are applied at the inlet. The outlet is set as the pressure-outlet boundary. Iron loss and copper loss calculated by the electromagnetic model as the heat source. Since the motorette is exposed to the external environment, a boundary condition with a natural convection coefficient of $20 \text{ W}/(\text{m}^2 \cdot ^\circ\text{C})$ is applied to its outer surface.

TABLE III

PHYSICAL PARAMETERS OF EACH COMPONENT IN THE FLUID-SOLID COUPLING MODEL

Properties	Iron core	Copper	Housing	Impregnation and insulation
Density [kg/m^3]	7600	8933	2790	1400
Specific heat capacity [$\text{J}/(\text{kg} \cdot ^\circ\text{C})$]	502	385	833	1400
Thermal Conductivity [$\text{W}/(\text{m} \cdot ^\circ\text{C})$]	20/20/3.6	398	168	0.24

TABLE IV

THE OIL PROPERTIES CHANGE WITH TEMPERATURE $T [^\circ\text{C}]$

Properties	Expression
Density [kg/m^3]	$\rho = 983.7096 - 0.70054T$
Specific heat capacity [$\text{J}/(\text{kg} \cdot ^\circ\text{C})$]	$C_p = 1946.13 + 2.75T$
Thermal conductivity [$\text{W}/(\text{m} \cdot ^\circ\text{C})$]	$\lambda_j = 0.15431 - 2.9952E-4T + 4.38737E-7T^2$
Kinematic viscosity [mm^2/s]	$\nu = 154.41266e^{-0.045627T}$

D. LPTN Model

The LPTN model is used to verify the applicability of the dimensionless correlations obtained by fitting the numerical analysis results. The convective thermal resistances of the front and rear end-windings are the key to the LPTN model. In addition, extremely accurate conduction thermal resistances are required to minimize the effect on the validated convective thermal resistances. The 3D thermal network captures the temperature gradient more precisely than the 2D thermal network. Considering the saving of computational resources and modeling time, a combined 2D and 3D LPTN model is adopted in this paper as shown in Fig. 8. The meanings of thermal resistances of the motorette are shown in Table V.

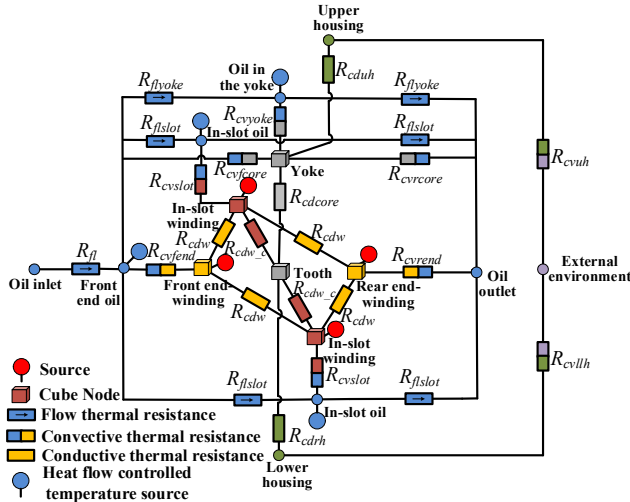


Fig. 8. The thermal network of the motorette.

The model contains 15 nodes representing the 15 main parts of the motorette and the cooling medium. Among them, a fluid flow network is constructed by 6 nodes, which are specifically simulated with 2D flow thermal resistance and heat flow controlled temperature sources. Since the housing is aluminum alloy with large thermal conductivity and small temperature gradient, only two 2D nodes are used to indicate the upper and lower housing, respectively. Meanwhile, one 2D node indicates the external ambient temperature, and there is natural convective thermal resistance between this node and the housing node. The core and winding are represented by two-node and four-node cubic models. The analysis above shows that there are two lower numbers in the anisotropic thermal conductivity of the winding. However, the oil flows over the surface of the winding with a strong convective heat transfer, which leads to a larger Biot number and temperature gradient [35]. Therefore, it is required to discrete the winding into 5 sections with lower thermal conductivity in each of the two directions. The in-slot winding and end-winding are each divided into 25 three-dimensional thermal circuit units. The connection of the in-slot winding and the end-winding is shown in Fig. 9, and the entire winding is discrete into 100 three-dimensional thermal circuit units.

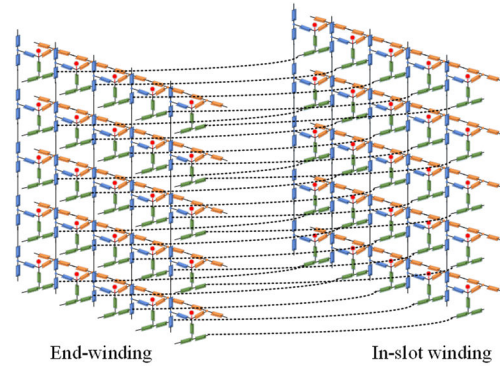


Fig. 9. Detailed 3D thermal network connection of end-winding and in-slot winding.

TABLE V
DEFINITION OF THERMAL RESISTANCES

Parameter	Meaning of Thermal Resistance
$R_{fl}, R_{flslot}, R_{flyoke}$	Thermal resistance to fluid flow in end spaces, slots and yoke passages
$R_{cvyfend}, R_{cvrend}$	Convective thermal resistance of front and rear end-windings
R_{cvslot}, R_{cvyoke}	Convective heat resistance in the slot and yoke
$R_{cvfcore}, R_{cvrcore}$	Convective thermal resistance of the front and rear end surfaces of the core
R_{cdw}	Conductive thermal resistance between in-slot winding and end-winding
R_{cdw_c}	Contact thermal resistance between in-slot winding and core
R_{cdcore}	Conductive thermal resistance between tooth and yoke
R_{cduh}, R_{cdrh}	Conductive thermal resistance of upper and lower housing
R_{cvuh}, R_{cvrh}	Natural convective thermal resistance of upper and lower housing

IV. CONVECTION HEAT TRANSFER CHARACTERISTICS OF END-WINDINGS

A. Temperature Field Analysis

Based on the above analysis, the numerical model of the

stator immersed oil-cooled motorette is solved by ANSYS Fluent. The temperature field and velocity streamlines of the single-tooth motorette at a current density of 22A/mm^2 and a flow rate of 3L/min are shown in Fig. 10. When oil enters the front end space, it directly impacts the front end-winding. The temperature of the outer surface of the front end-winding is low, which is the part of the winding with the best cooling effect, particularly the local area facing the inlet. On one hand, the winding in the slot removes heat through direct contact with oil. On the other hand, heat is transferred to the core via heat conduction. The temperature of the winding at the center of the slot is the highest, as shown by the temperature contour plot of the center cross section, and the temperature gradient of the winding is large. The oil flows directly to the outlet in the rear end space after exiting the oil passage in the yoke and slot, resulting in a much smaller impact effect of oil on the rear end-winding than the impact effect on the front end-winding. Its convection heat dissipation effect is poor, the average temperature of the rear end-winding is higher than that of the front end-winding, which is also a feature of the temperature distribution of the stator immersed oil-cooled electrical machine. Due to the longitudinal staggered oil passages, the temperature of the yoke is lower than that of the tooth. It can be seen from the iron core temperature contour plot that the temperature of the rear end is higher than the temperature of the front end, and the highest temperature of the iron core appears on the surface of the rear tooth.

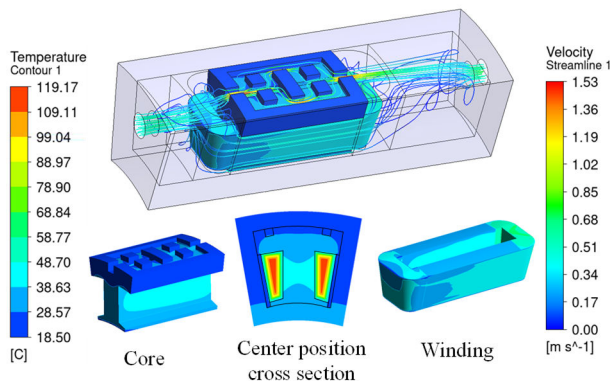


Fig. 10. Temperature field with inlet flow rate of 3L/min and current density of 22A/mm^2 .

Indirect slot cooling is as well considered as an efficient cooling technique [36], [37]. However, the coolant can only flow in the pipes, which prevents the end-windings and stator core from being adequately cooled. In addition, the contact thermal resistance between the winding and the pipe will further reduce the heat dissipation performance of the indirect slot cooling. As shown in Fig. 11, for the same loss and oil flow rate in the slot, the maximum temperature of the stator immersed oil-cooled electrical machine decreases by 31% compared to indirect slot cooling, which indicates that oil immersion cooling is more suitable for application in ultra-high power density electrical machines. Moreover, the oil immersion cooling with yoke oil passage can reduce the temperature of the core more effectively.

The straight yoke oil passage is a common cooling design for oil-cooled electrical machines. The advantage of the proposed longitudinal staggered yoke oil passage is that it increases the

contact area between the oil and the yoke, and increases the turbulence of the flow by the design of the bent oil passage, thus improving the convective heat transfer coefficient. As can be seen from Fig. 12, the longitudinal staggered oil passages have larger convective heat transfer coefficients at several corners of the oil passages, while the straight oil passages only have localized areas of larger convective coefficients near the inlet. However, the flow resistance of the longitudinal staggered oil passage is greater than that of the straight yoke oil passage. Hence, the inlet velocity distribution of the yoke oil passage in Fig. 12 shows that the flow rate in the longitudinal staggered oil passage is a slightly lower than that of the straight yoke oil passage. As shown in Fig. 13, the convective thermal resistance of the longitudinal staggered oil passage is about 55% to 60% lower than that of the straight oil passage.

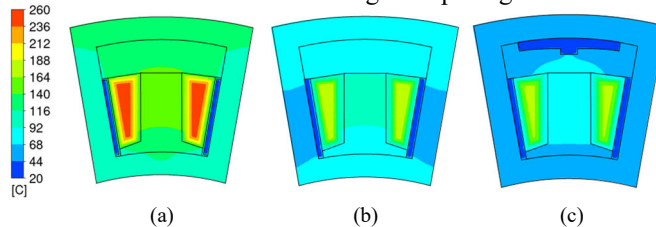


Fig. 11. Temperature field with inlet flow rate of 1L/min . (a) Indirect slot cooling. (b) Stator immersed oil cooling without yoke oil passage. (c) Stator immersed oil cooling with longitudinal staggered yoke oil passage.

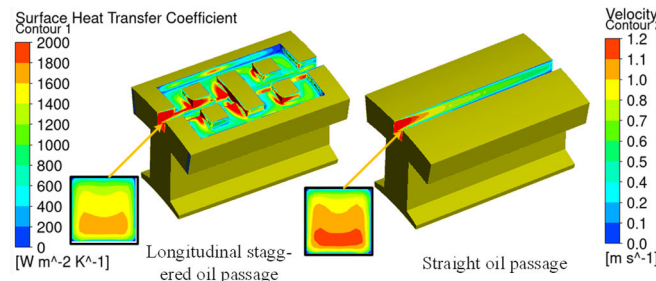


Fig. 12. The convective heat transfer coefficient distribution and cross-sectional flow velocity diagram of longitudinal staggered oil passage and straight oil passage with inlet flow rate of 3L/min .

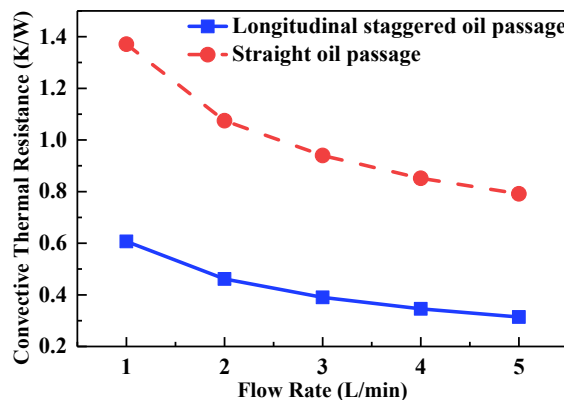


Fig. 13. The convection thermal resistance of yoke oil passages at different flow rates.

The ratio of copper loss and iron loss will vary under different working conditions of the electrical machine. In order to further investigate the efficient heat dissipation performance of the longitudinal staggered oil passages, different iron loss to copper loss ratios are analyzed. The temperature results of varying the iron loss at a flow rate of 1L/min with constant

copper loss are shown in Fig. 14. The core as well as winding temperature of the longitudinal staggered yoke oil passage is consistently lower than that of the straight yoke oil passage. The advantage of the longitudinal staggered yoke oil passage is more significant in the case of a higher percentage of iron loss, which can decrease the core temperature by 7%.

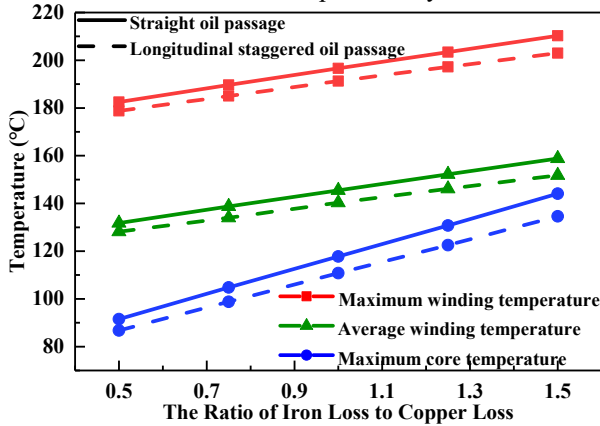


Fig. 14. The comparison of motorettes temperature of two different yoke oil passages with varying iron loss to copper loss ratio.

B. The CHTC of End-Winding

Convective heat transfer is the result of the combined effect of heat migration caused by fluid flow and heat transfer caused by heat conduction of molecules in the fluid. The following equation can be obtained from Fourier's law:

$$h = -\frac{\lambda}{\Delta t} \frac{\partial t}{\partial y} \Big|_{y=0} = \frac{q}{(T_s - T_{ref})} \quad (17)$$

where q is heat flux, T_s is the convective heat transfer surface temperature, T_{ref} the average temperature of local fluid on convective heat transfer surface. Considering that convective heat transfer is closely related to fluid flow, the fluid flow characteristics of the end-windings are studied first before analyzing the convective heat transfer characteristics. The oil flowing from the inlet directly impacts the front end-winding, and forming two tributaries, one flowing through the upper surface of the front end-winding into the yoke oil passage and the other flowing around the sides of the front end-winding into the oil passage in the slot, as shown in Fig. 15. It can be seen from Fig. 16 that the CHTC is greatest at the junction of surface F_{mid} and surface F_{top} of the front end-winding. Due to the blocking effect of the core, a small portion of the tributary flow into the yoke oil passage flows through the inner surface F_{ins} of the front end-winding. However, since its low flow rate, the surface F_{ins} is the area with the smallest CHTC for the entire front end-winding. The two tributaries converge after exiting the yoke oil passage and the in-slot oil passage, respectively, and flow directly to the outlet. It is obvious that the CHTC on the surface of the rear end-winding is lower than that on the surface of the front end-winding. It is worth noting that the fluid flow direction at the inner surface of the rear end-winding is from bottom to top due to the faster flow rate above the rear end region, which results in a lower pressure above. In terms of oil passage flow distribution, Fig. 17 shows that the overall ratio of in-slot oil passage flow rate to yoke oil passage flow rate is approximately 3:2, although an increase in flow rate slightly reduces the percentage of yoke oil passage flow rate.

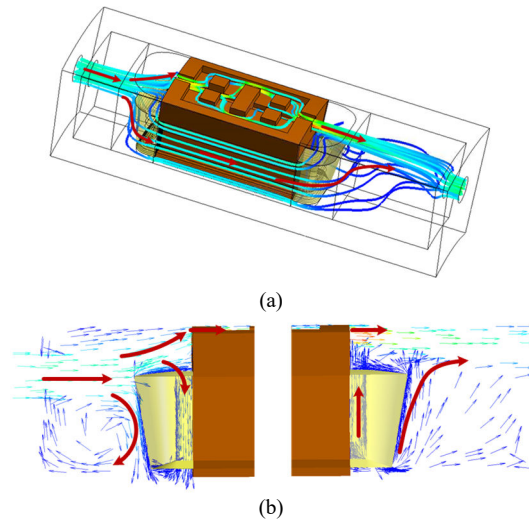


Fig. 15. The fluid flow in a single-tooth motorette. (a) Streamline diagram of the fluid. (b) Velocity vector at the center cross section.

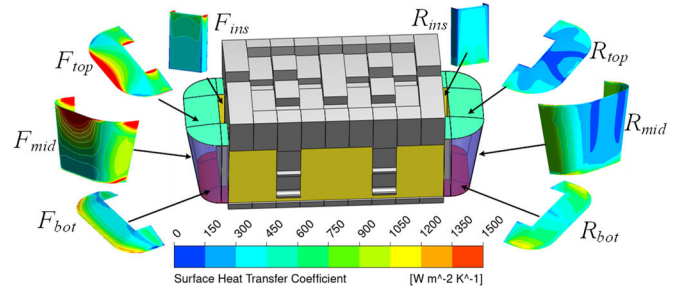


Fig. 16. The CHTC of each surface of the end-winding at a flow rate of 3L/min.

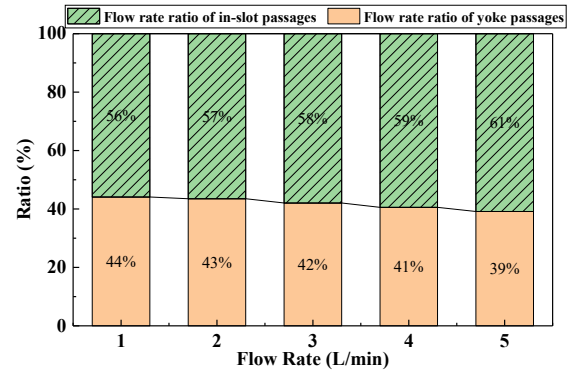


Fig. 17. The flow rate ratio of in-slot passages and yoke passages at different flow rates.

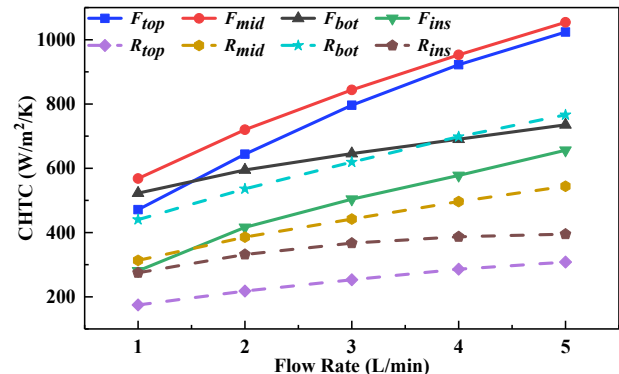


Fig. 18. The CHTC of each surface of the end-winding varies with the flow rate.

As shown in Fig. 18, the CHTCs of the four surfaces of the front end-winding are all higher than those of the four surfaces in the same position of the rear end-winding. The CHTC of each surface increases with increasing flow rate, and the increasing trend is more visible at low flow rate. After the flow rate reaches 4L/min, the increasing trend of CHTC decreases, and the convective heat dissipation effect tends to saturate.

In the actual thermal analysis of the electrical machine, usually only one convective thermal resistance is used to express the convective heat dissipation effect of the end-winding. Therefore, the convection heat transfer coefficients of the four surfaces of the end-windings at both ends are equivalent with the following equation:

$$h_{av} = \frac{\sum_{i=1}^4 h_i A_i}{\sum_{i=1}^4 A_i} \quad (18)$$

where A_i is the area of different heat exchange surfaces, h_{av} is the average CHTC. Fig. 19 shows that the average CHTC of the front end-winding is 65% to 90% higher than that of the rear end-winding as the flow rate increases. Since the front end-winding is subjected to oil impingement, it can be approximated as an oil impingement cooling problem. In the area of convective heat transfer for oil impingement cooling, C. F. Ma and J. E. Leland have done extensive experiments and summarized the relevant dimensionless correlations [38] [39]. In this paper, the oil inlet is equivalent to a nozzle, and its calculation results are shown in Fig. 19. It can be seen that the CHTC obtained by the empirical correlation of oil impingement cooling only correspond to the results of the new dimensionless correlation calculations under some specific operating conditions, and overall shows a low CHTC at low flow rates and a high convective coefficient at high flow rates. The difference between the CHTC calculated using the empirical correlation of oil impingement cooling and the new dimensionless correlation can be up to 40%. Furthermore, the empirical correlation of oil impingement cooling cannot predict the CHTC of the rear end-winding, with a substantial difference between the two, especially at high flow rates.

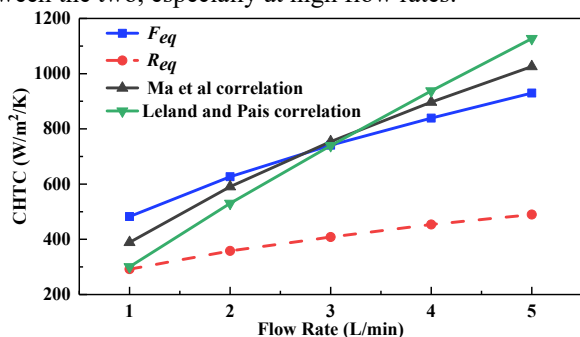


Fig. 19. The comparison of the average CHTC of the end-winding and the CHTC calculated by the empirical correlation for oil impingement cooling.

C. Dimensionless Analysis

The CHTC of the electrical machine is related to the fluid flow state, physical characteristics, end-winding geometry, roughness and the relative position of the heat exchange surface and the fluid. It is necessary to apply the principle of similarity

criterion for research. According to the dimensional analysis method, the following dimensionless numbers can be obtained:

$$Re = \frac{\rho u d}{\mu} \quad (19)$$

$$Nu = \frac{h d}{\lambda} \quad (20)$$

$$Pr = \frac{C_p \mu}{\lambda} \quad (21)$$

where u and d are the average flow velocity and equivalent diameter of the end space section of the stator immersed oil-cooled electrical machine, respectively. d is defined as:

$$d = r_{so} - r_{si} \quad (22)$$

where r_{so} and r_{si} are the outer and inner radii of the stator, respectively. In the study of the CHTC, the method of organizing data in the form of a power function with established criteria is usually used, namely:

$$Nu = a Re^b Pr^c \quad (23)$$

where a , b , c are the coefficients fitted according to the data. For the issue of the CHTC on the surface of the circular tube type, previous studies have shown that the coefficient c is generally adopted as 1/3 [40], [41]. The result of the fitting is shown in Fig. 20 and Table VI. It should be noted that the fitted dimensionless correlations are more relevant for stator immersed oil-cooled electrical machines with both yoke oil passages and in-slot oil passages. In order to make the correlation available for a broader range of designs, different l/d require to be analyzed. As shown in Fig. 20, the error between the calculated results of dimensionless correlation and simulation is close to 20% when l/d increases to 5. Therefore, the applicable range of dimensionless correlation can be limited to $0.2 < l/d < 5$ and $8 < Re < 41$.

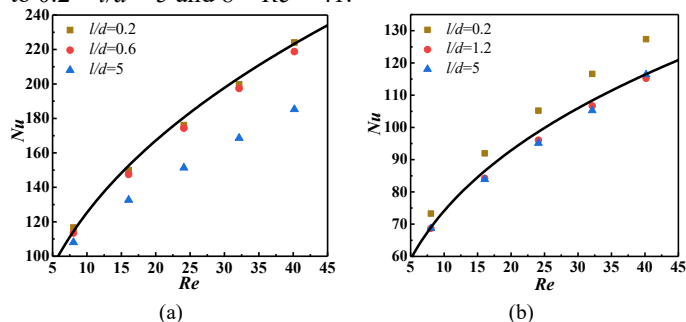


Fig. 20. The dimensionless correlation for fitting the CHTC of the end-winding. (a) Front end-winding. (b) Rear end-winding.

TABLE VI
COEFFICIENTS OF DIMENSIONLESS CORRELATIONS

Position	Coefficient a	Coefficient b	Coefficient c
Front end-winding	5.25	0.4155	1/3
Rear end-winding	3.821	0.3254	1/3

V. EXPERIMENTAL VALIDATIONS AND ANALYSIS OF RESULTS

A. Experimental Setup

The measurement setup and configuration of the stator immersed oil-cooled experimental platform is shown in Fig. 21. Integrated fuel tank and radiator pumps and cools the oil to

ensure that the oil temperature is maintained at a constant value at the inlet. The flow rate is measured using a turbine flow meter. Temperature sensors (PT100, $\pm 0.01^\circ\text{C}$) and pressure gauges (0.6MPa, $\pm 3\text{Pa}$) are installed at the inlet and outlet to measure the temperature rise and pressure drop of the oil. It is worth noting that the pressure gauge requires to be placed as close as possible to the inlet and outlet positions. This is due to its distance from the inlet and outlet as well as the conduit bends that can lead to larger errors in the pressure drop between experiment and simulation. The motorette is powered by a DC power supply. It is worth noting that the windings of the motorette are coated with a thin layer of thermally conductive adhesive on the outer surface after impregnation to avoid damage to the insulation of the windings by the long-term impact of the oil. The effect of this part on heat transfer should be attributed to the outermost impregnation and insulation equivalent layer using the equation for calculating the thermal conductivity of composite materials.

Six PT100 temperature sensors of smaller size (3mm*2mm) are installed in the motorette to correctly obtain the distribution of the temperature field, as shown in Fig. 22. In order to measure the maximum temperature of the winding, temperature sensors are placed in the center of the front end-winding, the in-slot winding and the rear end-winding. Two temperature sensors are also placed on the surface of the tooth and yoke of the core, respectively. The average temperature of the winding is more difficult to measure, but the loss can be measured on the DC power supply so that the resistance can be calculated. The average temperature of the winding can be roughly estimated using the following equation:

$$T_{avg} = \left(\frac{R_w A_w}{l_w \rho_{15}} - 1 \right) / \beta + 15 \quad (24)$$

where l_w and A_w are the length and cross-sectional area of the conductor, respectively. R_w is the winding resistance. ρ_{15} is the resistivity of copper at a temperature of 15°C . β is the temperature coefficient of resistance of the conductor.

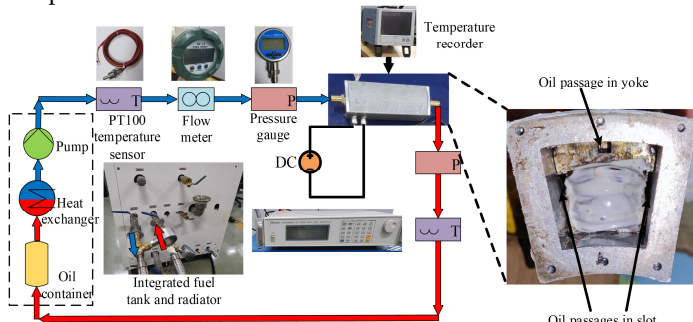


Fig. 21. Test setup and configuration of the stator immersed oil-cooled experimental platform.

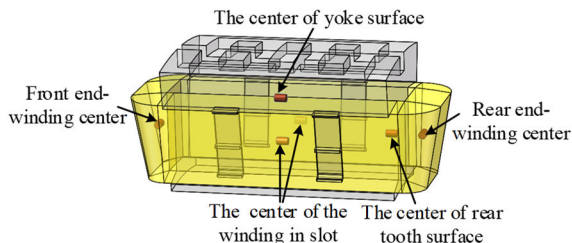


Fig. 22. Test distribution of temperature sensors in the motorette.

B. Comparison of Simulated and Measured Values

The results of the experiments and CFD simulations are shown in Fig. 23 (a). Specifically, the differences between the front end-winding and rear end-winding temperatures are compared and are consistent with the previous analysis that the rear end-winding temperature is higher than the front-end winding temperature. The temperature of the core from the CFD simulation is almost the same as the experimentally measured data. The largest error is the average temperature of the winding, which is mainly due to the following two reasons. On one hand, the losses recorded on the DC power supply are the total losses of the whole system. Due to natural cooling, the temperature at the joints of the winding wires and the power supply wires is greater under high currents, resulting in increased losses here. The effect of this aspect is ignored in the simulation, and the loss density is set slightly higher. Therefore, the simulation temperature is high compared to the experimental temperature. On the other hand, the results calculated using Eq. (24) can only be used as a rough estimate of the average winding temperature, where the evaluation of the winding length parameter is also subject to some error. The highest error of the maximum winding temperature obtained from simulation and experiment is within 10°C , indicating that the previous simulation analysis is correct. It is worth noting that the error increases as the flow rate increases. This may be due to the smoother winding surface modeled by the simulation. The actual winding surface has some degree of unevenness, which can lead to an enhanced convective heat transfer effect at high flow rates, thus further reducing the winding temperature.

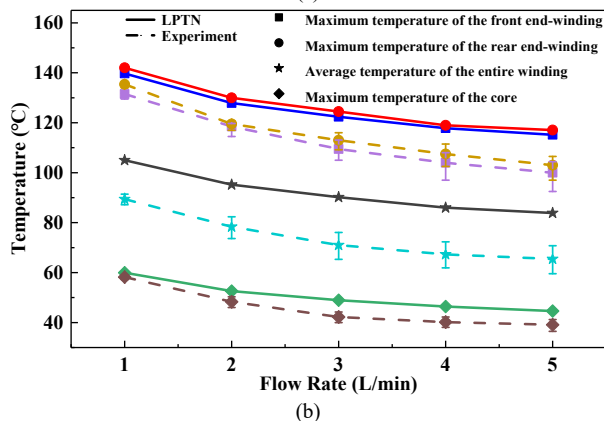
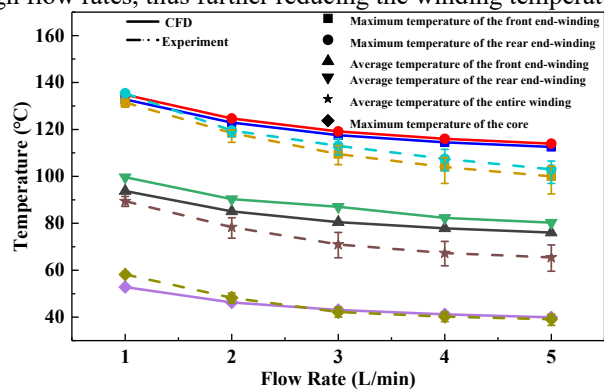


Fig. 23. The comparison of simulation and experimental results for a current density of $22\text{A}/\text{mm}^2$. (a) The comparison between CFD and experiment. (b) The comparison between LPTN and experiment.

To verify whether the dimensionless correlation summarized in the previous section can be used in the thermal network for fast temperature field calculation, the CHTC calculated by the dimensionless correlation is brought into the thermal network model, and the results are shown in Fig. 23 (b). Since the thermal network is a lumped parameter model, although the windings have been equated with 100 3D cube models, the concentration of heat sources makes the error between them and the experiment higher than the error between CFD and the experiment. The errors between the simulated and experimental maximum winding and core temperatures are within 15°C and 5°C, respectively, indicating that the dimensionless correlations can be used for the evaluation of the CHTCs of the end-winding during the initial design of stator immersed oil-cooled electrical machines. In order to test the cooling performance of this stator immersed oil-cooled structure, different currents are applied to the winding at moderate flow rates, as shown in Fig. 24. The maximum current density allowed by this cooling structure is up to 30A/mm².

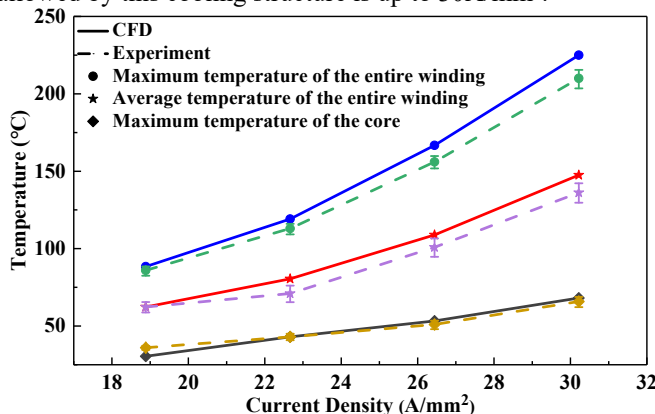


Fig. 24. Variation of motorette temperature with winding current density at a flow rate of 3L/min.

C. Influence of Inlet Temperature

As can be seen from Table IV, the physical properties of the aviation lubricants used in this paper are sensitive to temperature, especially viscosity. When the temperature increases from room temperature, the viscosity of the oil drops sharply. As shown in Fig. 25, increasing the inlet temperature improves the convective heat transfer performance of the front end-winding by about 15% at most. However, since the rear end-winding is not subject to the impinge effect of the winding, the inlet temperature change has little effect on the convective heat transfer performance of the rear end-winding.

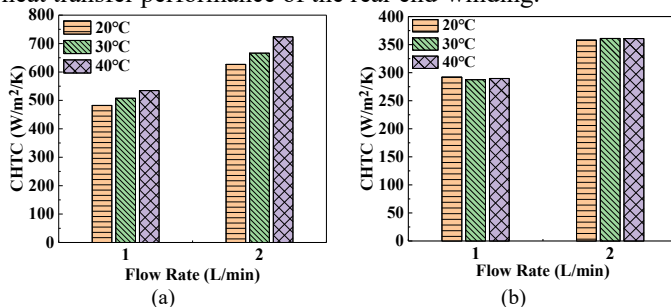


Fig. 25. The average convection heat transfer coefficient of end-winding at different inlet temperatures. (a) Front end-winding. (b) Rear end-winding.

D. Influence of Power Loss

The power loss has no direct effect on convective heat transfer, but the properties of the oil used in this paper are closely related to the temperature. High power losses lead to high surface temperature of the winding, the fluid viscosity near the fluid-solid coupling surface decreases sharply, and the convective heat transfer effect is enhanced. As shown in Fig. 26, the average CHTCs of both front and rear end-winding surfaces increase with the increase of current density. Since the rear end-winding is less affected by the impact of oil, the tendency of its CHTC to increase with current density is lower than that of the CHTC of the front end-winding. It is worth noting that the effect of the power loss on the CHTC is higher than the effect of the inlet temperature on the CHTC. This is due to the fact that the increase in inlet temperature makes the thermal conductivity of the whole fluid decrease, which inhibits the tendency of convective heat transfer enhancement to some extent. To evaluate the effect of power loss variation on the dimensionless correlation, the error is included in Table VII. The maximum error is 8.7% for the front end-winding and 9.7% for the rear end-winding, which further verifies the accuracy of the dimensionless correlation.

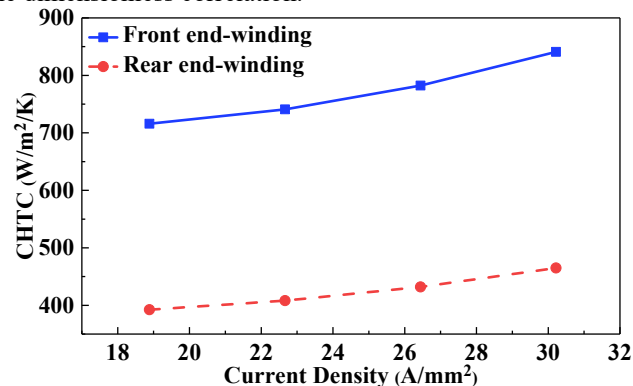


Fig. 26. The variation of the average CHTC of the end-winding with current density at a flow rate of 3L/min.

TABLE VII
NUSSELT NUMBER FOR EXPERIMENTS AND SIMULATIONS AT DIFFERENT CURRENT DENSITIES

Current density [A/mm ²]	Front end-winding			Rear end-winding		
	Nu_{exp}	$Nu_{correlation}$	error [%]	Nu_{exp}	$Nu_{correlation}$	error [%]
18.9	168.4		7.2	92.3		6.9
22.6	174.5	180.6	3.5	96.1	98.7	2.7
26.4	184.1		1.9	101.6		2.8
30.2	197.9		8.7	109.4		9.7

VI. CONCLUSION

In this paper, the heat dissipation mechanism and the convective heat transfer characteristics of the end-windings for stator immersed oil-cooled electrical machines with yoke oil passages and in-slot oil passages were investigated. A CFD-based numerical model was developed to achieve an accurate description of the temperature distribution and the CHTC of the end-windings. Based on the numerical data, new dimensionless correlations were defined and applied in the calculation of the convective thermal resistance of the end-windings for the LPTN model. The conclusions can be drawn as follows:

1) The numerical data shows that the CHTCs of both front and rear end-windings increase with the flow rate. However, its growth trend gradually decreases with the increase in the flow rate, and the cooling effect tends to saturate at high flow rates. The convective heat transfer effect of the front end-winding is significantly stronger, and its CHTC is 1.65 to 1.9 times higher than that of the rear end-winding as the flow rate increases.

2) The difference between the CHTC calculated with the empirical dimensionless correlation of oil impingement cooling and the new dimensionless correlation is up to 40%. Furthermore, the empirical correlation of oil impingement cooling cannot reflect the significant difference in convective heat transfer characteristics of the front and rear end-windings.

3) The increase of inlet oil temperature or power loss can improve the CHTC of the end-windings. However, compared with the new dimensionless correlation calculation, the error is within 10% based on the existing experimental results.

4) The numerical data and the thermal circuit results are validated using experimental data, which shows that the error in temperature estimation is within 15%. In addition, experiments demonstrate that the cooling structure presented in this paper can withstand a current density of up to 30A/mm².

The convective heat transfer characteristics of the end-windings are closely related to the design of the stator immersed oil-cooled structure. The dimensionless correlations proposed herein may provide a reference for researchers in this field to design stator immersed oil-cooled machines with structures similar to those in this paper. The convective heat transfer characteristics of end-windings with different stator immersed oil-cooled structures will be investigated in the future.

REFERENCES

- [1] W. Cao, B. C. Mecrow, G. J. Atkinson, J. W. Bennett and D. J. Atkinson, "Overview of electric motor technologies used for more electric aircraft (MEA)," *IEEE Trans. Ind. Electron.*, vol. 59, no. 9, pp. 3523-3531, Sept. 2012.
- [2] X. Zhang and K. S. Haran, "High-specific-power electric machines for electrified transportation applications-technology options," in *IEEE Energy Convers. Congr. Expo. (ECCE)*, 2016, pp. 1-8.
- [3] X. Fan, D. Li, R. Qu, C. Wang and H. Fang, "Water cold plates for efficient cooling: verified on a permanent-magnet machine with concentrated winding," *IEEE Trans. Ind. Electron.*, vol. 67, no. 7, pp. 5325-5336, July 2020.
- [4] N. None, *Electrification FY2018 Annual Progress Report*. Accessed on: Oct 3rd, 2019. [Online]. Available: <https://www.energy.gov/eere/vehicles/downloads/electrification-fy2018-annual-progress-report>.
- [5] X. Zhang, C. L. Bowman, T. C. O'Connell and K. S. Haran, "Large electric machines for aircraft electric propulsion," *IET Electr. Power Appl.*, vol. 12, no. 6, pp. 767-779, July 2018.
- [6] G. C. Montanari, G. Mazzanti and L. Simoni, "Progress in electrothermal life modeling of electrical insulation during the last decades," *IEEE Trans. Dielect. Elect. Insul.*, vol. 9, no. 5, pp. 730-745, Oct. 2002
- [7] A. Lindner, K. Litvinova, G. Popov and I. Hahn, "Measurement of rare earth magnets at high temperatures," in *Int. Symp. Power Electron., Elect. Drives, Automat. Motion (SPEEDAM)*, 2016, pp. 213-220.
- [8] X. Fan, D. Li, R. Qu and C. Wang, "A dynamic multilayer winding thermal model for electrical machines with concentrated windings," *IEEE Trans. Ind. Electron.*, vol. 66, no. 8, pp. 6189-6199, Aug. 2019.
- [9] P. Lindh *et al.*, "Direct liquid cooling method verified with an axial-flux permanent-magnet traction machine prototype," *IEEE Trans. Ind. Electron.*, vol. 64, no. 8, pp. 6086-6095, Aug. 2017.
- [10] Y. Gai *et al.*, "Cooling of automotive traction motors: schemes, examples, and computation methods," *IEEE Trans. Ind. Electron.*, vol. 66, no. 3, pp. 1681-1692, March 2019.
- [11] C. Dong, Y. Qian, Y. Zhang and W. Zhuge, "A review of thermal designs for improving power density in electrical machines," *IEEE Trans. Transp. Electric.*, vol. 6, no. 4, pp. 1386-1400, Dec. 2020.
- [12] B. Li, H. Kuo, X. Wang *et al.* "Thermal management of electrified propulsion system for low-carbon vehicles," *Automot. Innov.*, vol. 3, no. 4, pp. 299-316, Dec. 2020.
- [13] M. Popescu, D. A. Staton, A. Boglietti, A. Cavagnino, D. Hawkins and J. Goss, "Modern heat extraction systems for power traction machines—a review," *IEEE Trans. Ind. Appl.*, vol. 52, no. 3, pp. 2167-2175, May-June 2016.
- [14] P. -O. Gronwald and T. A. Kern, "Traction motor cooling systems: a literature review and comparative study," *IEEE Trans. Transp. Electric.*, vol. 7, no. 4, pp. 2892-2913, Dec. 2021.
- [15] F. R. Ismagilov, V. E. Vavilov and D. V. Gusakov, "High-speed starter-generator for aerospace applications: design and initial testing," in *XIII Int. Conf. Elect. Mach. (ICEM)*, 2018, pp. 2593-2599.
- [16] T. Davin, J. Pellé, S. Harmand and R. Yu, "Experimental study of oil cooling systems for electric motors," *Appl. Therm. Eng.*, vol. 75, no. , pp. 1-13, Jan. 2015.
- [17] K. Lee, H. Cha, Y. Kim, "Development of an interior permanent magnet motor through rotor cooling for electric vehicles," *Appl. Therm. Eng.*, vol. 95, no. pp. 348-356, Feb. 2016.
- [18] Z. Li, L. Ruan and L. Tang, "Heat transfer characteristics of spray evaporative cooling system for large electrical machines," in *Int. Conf. Elect. Mach. Syst. (ICEMS)*, 2015, pp. 1740-1743.
- [19] A. Al-Timimy *et al.*, "Design and losses analysis of a high power density machine for flooded pump applications," *IEEE Trans. Ind. Appl.*, vol. 54, no. 4, pp. 3260-3270, July-Aug. 2018.
- [20] F. R. Ismagilov, V. E. Vavilov and D. V. Gusakov, "Design features of liquid-cooled aviation starter generators," in *2018 IEEE Int. Conf. Elect. Syst. for Aircr., Railway, Ship Propulsion and Road Vehicles & Int. Transp. Electrification Conf. (ESARS-ITEC)*, 2018, pp. 1-5.
- [21] A. L. Rocca *et al.*, "Thermal management of a high speed permanent magnet machine for an aeroengine," in *Int. Conf. Elect. Mach. (ICEM)*, 2016, pp. 2732-2737.
- [22] K. Bennion, *Electric Motor Thermal Management*. Accessed on: June, 2 017. [Online]. Available: <https://www.nrel.gov/docs/fy17osti/68076.pdf>.
- [23] C. Liu *et al.*, "Experimental investigation on oil spray cooling with hairpin windings," *IEEE Trans. Ind. Electron.*, vol. 67, no. 9, pp. 7343-7353, Sept. 2020.
- [24] S. Kapatral, O. Iqbal, and P. Modi, "Numerical modeling of direct oil-cooled electric motor for effective thermal management," in *SAE World Congr.*, 2020.
- [25] N. Simpson, R. Wrobel, and P. H. Mellor, "Estimation of equivalent thermal parameters of impregnated electrical windings," *IEEE Trans. Ind. Appl.*, vol. 49, no. 6, pp. 2505-2515, Nov./Dec. 2013.
- [26] R. Wrobel and P. H. Mellor, "A general cuboidal element for three-dimensional thermal modelling," *IEEE Trans. Magn.*, vol. 46, no. 8, pp. 3197-3200, Aug. 2010.
- [27] R. C. Progelhof, J. L. Throne, and R. R. Ruetsch, "Methods for predicting the thermal conductivity of composite systems: A review," *Polym. Eng. Sci.*, vol. 16, no. 9, pp. 615-625, Sep. 1976.
- [28] N. Simpson, R. Wrobel and P. H. Mellor, "A general arc-segment element for three-dimensional thermal modeling," *IEEE Trans. Magn.*, vol. 50, no. 2, pp. 265-268, Feb. 2014.
- [29] Z. Sun, Q. Wang, G. Li, Z. Qian, W. Li and J. Jing, "A closed-Form analytical method for reliable estimation of equivalent thermal conductivity of windings with round-profile conductors," *IEEE Trans. Energy Convers.*, vol. 36, no. 2, pp. 1143-1155, June 2021.
- [30] D. Staton, A. Boglietti, and A. Cavagnino, "Solving the more difficult aspects of electric motor thermal analysis in small and medium size industrial induction motors," *IEEE Trans. Energy Convers.*, vol. 20, no. 3, pp. 620 - 628, Sep. 2005.
- [31] A. Fasquelle and D. Laloy, "Water cold plates cooling in a permanent magnet synchronous motor," *IEEE Trans. Ind. Appl.*, vol. 53, no. 5, pp. 4406- 4413, Sep./Oct. 2017.
- [32] R. Wrobel, G. Vainel, C. Copeland, T. Duda, D. Staton, and P. H. Mellor, "Investigation of mechanical loss components and heat transfer in an axialflux PM machine," *IEEE Trans. Ind. Appl.*, vol. 51, no. 4, pp. 3000-3011, Jul./Aug. 2015.
- [33] Y. Gai *et al.*, "On the measurement and modeling of the heat transfer coefficient of a hollow-shaft rotary cooling system for a traction motor," *IEEE Trans. Ind. Appl.*, vol. 54, no. 6, pp. 5978-5987, Nov./Dec. 2018.

- [34] F. R. Menter, "Two-equation eddy-viscosity turbulence models for engineering applications," *AIAA J.*, vol. 32, pp. 1598–1605, 1994.
- [35] P. Romanazzi, V. Galizzi, F. Carbone, A. Miotto and D. A. Howey, "Improved thermal equivalent circuit element applied to an external rotor SPM machine," in *Int. Conf. Elect. Mach. (ICEM)*, 2016, pp. 2718-2724.
- [36] M. Schiefer and M. Doppelbauer, "Indirect slot cooling for high-power density machines with concentrated winding," in *Proc. IEEE Int. Elect. Mach. Drives Conf.*, May 2015, pp. 1820–1825.
- [37] F. Zhang *et al.*, "Improved thermal modeling and experimental validation of oil-flooded high-performance machines with slot-channel cooling," in *IEEE Trans. Transp. Electrific.*, vol. 8, no. 1, pp. 312-324, Mar. 2022.
- [38] C. F. Ma, Q. Zheng, and S. Y. Ko, "Local heat transfer and recovery factor with impinging free-surface circular jets of transformer oil," *Int. J. Heat Mass Transf.*, vol. 40, no. 18, pp. 4295 – 4308, Mar. 1997.
- [39] J. E. Leland, and M. R. Pais, "Free jet impingement heat transfer of a high Prandtl number fluid under conditions of highly varying properties," *J. Heat Transf.*, vol. 121, no. 3, pp. 592 – 597, Aug. 1999.
- [40] F. P. Incropera, "Fundamentals of heat and mass transfer," ed: John Wiley & Sons, Inc., 2006.
- [41] J. Montonen, J. Nerg, M. Polikarpova, and J. Pyrhönen, "Integration principles and thermal analysis of an oil-cooled and -lubricated permanent magnet motor planetary gearbox drive system," *IEEE Access*, vol. 7, pp. 69108-69118, May 2019.



Runyu Wang was born in Anhui, China. He received the B.Eng. degree in electrical engineering and automation from Anhui University, Hefei, China, in 2019. He is currently working toward the Ph.D. degree in Huazhong University of Science and Technology, Wuhan, China. His research interests include electromagnetic and cooling design of high power density permanent magnet machines.



Xinggang Fan (Member, IEEE) was born in Hubei, China. He received the B.Eng. degree in energy engineering and Ph.D. degree in electrical engineering from Huazhong University of Science and Technology, Wuhan, China, in 2014 and 2019, respectively. He is currently a Postdoctoral Fellow with this university. His research interests include electromagnetic-thermal design and analysis of permanent magnet machines, especially those working in the high-power density occasions.



Dawei Li (Senior Member, IEEE) was born in China. He received the B.Eng. degrees in electrical engineering from Harbin Institute of Technology, Harbin, China, in 2010, and Ph.D. degree in electrical engineering, from Huazhong University of Science and Technology, Wuhan, China, in 2015. His research interests include design and analysis of novel permanent-magnet brushless machines.



Ronghai Qu (Fellow, IEEE) was born in China. He received the B.E.E. and M.S.E.E. degrees from Tsinghua University, Beijing, China, in 1993 and 1996, respectively, and the Ph.D. degree from the University of Wisconsin Madison, Madison, WI, USA, in 2002, all in electrical engineering.

In 1998, he joined the Wisconsin Electric Machines and Power Electronics Consortiums as Research Assistant. He became a Senior Electrical Engineer with Northland, a Scott Fetzer Company in 2002. Since 2003, he had been with the General Electric (GE) Global Research Center, Niskayuna, NY, as a Senior Electrical Engineer with the Electrical Machines and Drives Laboratory. He has authored over 120 published technical papers and is the holder of over 50 patents/patent applications. From 2010, he has been a professor with Huazhong University of Science & Technology, Wuhan, China.

Dr. Qu is also a Full Member of Sigma Xi. He received several awards from the GE Global Research Center Since 2003, including the Technical Achievement and Management Awards. He also received the 2003 and 2005 Best Paper Awards, Third Prize, from the Electric Machines Committee of the

IEEE Industry Applications Society (IAS) at the 2002 and 2004 IAS Annual Meeting, respectively.



Lei Li was born in Shandong, China. He received the B.Eng. degree in electrical engineering from China University of Mining and Technology, Xuzhou, China, in 2021. He is currently working toward the master's degree in electrical engineering at the Huazhong University of Science and Technology, Wuhan, China. His research interests include the design of permanent magnet machines and analysis of thermal.



Tianjie Zou (Member, IEEE) was born in Hubei, China, in 1991. He received the B.Sc. degree in electrical and electronic engineering and the Ph.D. degree in electrical engineering from the Huazhong University of Science and Technology, Wuhan, China, in 2013 and 2018, respectively. He joined the Power Electronics, Machines and Control (PEMC) Group, University of Nottingham, Nottingham, U.K., in 2018, as a Research Fellow. In 2020, he was awarded the Nottingham Research Fellowship and started his independent research career. His main research interests include the design, analysis, and intelligent control of permanent-magnet machines.

Dr. Zou was a recipient of the Best Paper Award in the 22nd International Conference on Electrical Machines (ICEM 2016).